Geophys. J. Int. (1999) **137,** 805–815

Three-dimensional sensitivity kernels for finite-frequency traveltimes: the banana–doughnut paradox

Henk Marquering,* F. A. Dahlen and Guust Nolet

Department of Geosciences, Princeton University, Princeton, NJ 08544, *USA. E-mail: tony@geo.princeton.edu*

Accepted 1999 January 15. Received 1999 January 2; in original form 1998 February 18

SUMMARY

We use a coupled surface wave version of the Born approximation to compute the 3-D sensitivity kernel $K_T(\mathbf{r})$ of a seismic body wave traveltime T measured by cross-correlation of a broad-band waveform with a spherical earth synthetic seismogram. The geometry of a teleseismic S wave kernel is, at first sight, extremely paradoxical: the sensitivity is zero everywhere along the geometrical ray! The shape of the kernel resembles that of a hollow banana; in a cross-section perpendicular to the ray, the shape resembles a doughnut. The cross-path extent of such a *banana–doughnut kernel* depends upon the frequency content of the wave. The kernel for a very high-frequency wave is a very skinny hollow banana; wave-speed heterogeneity wider than this banana affects the traveltime, in accordance with ray theory. We also use the Born approximation to compute the sensitivity kernel $K_{\Delta T}(\mathbf{r})$ of a differential traveltime ΔT measured by cross-correlation of two phases, such as SS and S, at the same receiver. The geometries of both an absolute SS wave kernel and a differential SS–S kernel are extremely complicated, particularly in the vicinity of the surface reflection point and the source-to-receiver and receiver-to-source caustics, because of the minimax character of the SS wave. Heterogeneity in the vicinity of the source and receiver exerts a negligible influence upon an SS–S differential traveltime ΔT only if it is smooth.

Key words: Fréchet derivatives, inhomogeneous media, S waves, tomography, traveltime, wave propagation.

1 INTRODUCTION

In seismic traveltime tomography, it is commonly assumed that the arrival time of a body wave phase depends only upon the wave speed along the geometrical ray path between the source and receiver. In fact, ray theory is only an infinite-frequency approximation; scattering and diffraction effects render the traveltimes of finite-frequency waves sensitive to 3-D structure off the ray. In traditional seismological practice, an analyst measures the traveltime of a phase by hand-picking the first break; the use of ray theory is generally justified by the argument that such a picked time corresponds to the arrival of the very highest-frequency waves. The widespread availability of broad-band digital data has led to the recent development of automated traveltime measurement techniques, based upon the cross-correlation of an observed body wave phase with the corresponding spherical earth synthetic phase. Cross-correlation methods have also been used to measure the relative arrival times of a phase at a number of stations in a seismic array (VanDecar & Crosson 1990) and the differential traveltime of two phases at the same station (e.g. Kuo *et al.* 1987; Sheehan & Solomon 1991; Woodward & Masters 1991). We formulate a procedure for interpreting such finite-frequency, cross-correlation traveltime measurements in this paper. The foundation for the method is a coupled surface wave version of the Born approximation, which we have previously used to study the 3-D sensitivity of seismic waveforms (Marquering *et al.* 1998). To determine a 3-D sensitivity kernel for an absolute or differential traveltime, it is simply necessary to represent such a measurement as a functional of the first-order waveform perturbation.

* Now at: Océ Technologies B.V., St. Urbanusweg 43, 5900 MA Venlo, the Netherlands.

2 THEORY

To focus the discussion, we restrict consideration to a teleseismic phase such as S, SS or ScS in an earth model whose shear wave speed is of the form $\beta(r)+\delta\beta(\mathbf{r})$, where $r=\|\mathbf{r}\|$ is the radial distance from the centre. The quantity $\delta\beta(\mathbf{r})$ represents a 3-D perturbation away from a spherically symmetric earth model $\beta(r)$; we shall assume that this perturbation is slight, in the sense

$$|\delta\beta(\mathbf{r})| \ll |\beta(r)| \,. \tag{1}$$

Let T be the theoretical traveltime of an S, SS or ScS wave in the unperturbed spherical earth. The first-order traveltime difference $\delta T = T_{\rm obs} - T$ is given, in the ray-theoretical approximation, by

$$\delta T = -\int_{\rm ray} \beta^{-2}(r)\delta\beta(\mathbf{r})\,ds\,, \tag{2}$$

where ds is the differential arclength along the ray. Eq. (2) is the basis of essentially all global traveltime tomography; Fermat's principle allows the integration to be performed along the unperturbed ray path in the spherical earth. We seek a more general first-order relation between δT and $\delta\beta(\mathbf{r})$, which accounts for the finite-frequency effect of off-path structure. Strictly speaking, 3-D perturbations to the compressional wave speed $\alpha(r)$ and the density $\rho(r)$ will affect the traveltime of a finite-frequency shear wave as well; in this paper, we ignore such perturbations, for simplicity.

2.1 Cross-correlation traveltime measurement

We begin by considering the simplest case—the measurement of an absolute shear wave traveltime by cross-correlation of an observed seismogram with a synthetic spherical earth seismogram. Let $u_{\rm obs}(t)$ denote an S, SS or ScS signal that arrives during a time interval $t_1 \le t \le t_2$, and let $u(t)$ be the corresponding synthetic signal. The latter spherical earth waveform may be computed in any desired manner; we employ fundamental and higher-mode surface wave summation. We define the cross-correlagram of the observed and synthetic pulses by

$$C(\tau) = \int_{t_1}^{t_2} u(t-\tau)u_{\rm obs}(t)\,dt\,. \tag{3}$$

The slightness (1) of the 3-D heterogeneity of the Earth guarantees that the observed pulse will differ from the synthetic pulse by an infinitesimally small perturbation:

$$u_{\rm obs}(t) = u(t) + \delta u(t)\,, \quad \text{where} \quad |\delta u(t)| \ll |u(t)|\,. \tag{4}$$

The cross-correlation (3) may likewise be decomposed into a zeroth-order and a first-order term:

$$C(\tau) = c(\tau) + \delta c(\tau)\,, \tag{5}$$

where

$$c(\tau) = \int_{t_1}^{t_2} u(t-\tau)u(t)\,dt\,, \tag{6}$$

$$\delta c(\tau) = \int_{t_1}^{t_2} u(t-\tau)\delta u(t)\,dt\,. \tag{7}$$

In applications, the traveltime shift $\delta T = T_{\rm obs} - T$ of the observed phase $u_{\rm obs}(t)$ with respect to the synthetic $u(t)$ is determined by finding the maximum of $C(\tau)$. The unperturbed cross-correlation $c(\tau)$ obviously attains its maximum at zero lag: $\partial_\tau c(0) = 0$. In the vicinity of this unperturbed maximum, we can expand (5) in a Taylor series, keeping terms of second order in the peak shift $\delta\tau$:

$$\begin{aligned} C(\delta\tau) &= c(0) + \delta\tau\partial_\tau c(0) + \frac{1}{2}\,\delta\tau^2\partial_{\tau\tau}c(0) + \delta c(0) + \delta\tau\partial_\tau\delta c(0) \\ &= c(0) + \frac{1}{2}\,\delta\tau^2\partial_{\tau\tau}c(0) + \delta c(0) + \delta\tau\partial_\tau\delta c(0)\,. \end{aligned} \tag{8}$$

To find the shift in the position of the maximum we differentiate (8) with respect to $\delta\tau$ and set the result equal to zero:

$$\partial_{\delta\tau}\left[c(0) + \frac{1}{2}\,\delta\tau^2\partial_{\tau\tau}c(0) + \delta c(0) + \delta\tau\partial_\tau\delta c(0)\right] = 0\,, \tag{9}$$

or, equivalently,

$$\delta\tau = -\frac{\partial_\tau\delta c(0)}{\partial_{\tau\tau}c(0)}\,. \tag{10}$$

Upon carrying out the indicated operations in (10) and making the identification $\delta\tau = \delta T$, in accordance with our sign and 'which signal is lagged' conventions in eq. (3), we obtain an explicit expression for the cross-correlation traveltime shift:

$$\delta T = \frac{\displaystyle\int_{t_1}^{t_2} \dot{u}(t)\delta u(t)\,dt}{\displaystyle\int_{t_1}^{t_2} \ddot{u}(t)u(t)\,dt}\,, \tag{11}$$

where a dot denotes differentiation with respect to time. A *negative* traveltime shift, $\delta T < 0$, corresponds to an *advance* in the arrival of the observed signal $u_{\rm obs}(t)$ with respect to the synthetic signal $u(t)$, whereas a *positive* traveltime shift, $\delta T > 0$, corresponds to a *delay*.

2.2 Waveform sensitivity kernel

The Born approximation allows us to express the first-order sensitivity of the perturbation $\delta u(t)$ to the 3-D heterogeneity $\delta\beta(\mathbf{r})$ in the form

$$\delta u(t) = \int_\oplus K_u(\mathbf{r}, t)\,\delta\beta(\mathbf{r})\,dV\,, \tag{12}$$

where the integration is over all points $\mathbf{r}$ within the earth $\oplus$, and the subscript serves as a reminder that $K_u(\mathbf{r}, t)$ is the Fréchet kernel for the waveform. In the formulation of Marquering *et al.* (1998) the kernel in (12) is expressed as a sum over all minor-arc surface waves of the form

$$\begin{aligned} K_u(\mathbf{r}, t) = \frac{1}{\pi}\,\mathcal{R}e \int_0^\infty \sum_{n,n'} R_n(\omega) &\left\{\frac{\exp i\,[k_n(\omega)\Delta_{\rm r}(\mathbf{r}) + \pi/4]}{\sqrt{\frac{1}{2}\,\pi k_n(\omega)\sin\Delta_{\rm r}(\mathbf{r})}}\right\} \\ \times V_{nn'}(\mathbf{r}, \omega) &\left\{\frac{\exp i\,[k_{n'}(\omega)\Delta_{\rm s}(\mathbf{s}) + \pi/4]}{\sqrt{\frac{1}{2}\,\pi k_{n'}(\omega)\sin\Delta_{\rm s}(\mathbf{r})}}\right\} S_{n'}(\omega) \\ \times \exp(-i\omega t)\,d\omega\,. \end{aligned} \tag{13}$$

The frequency-dependent terms in the inverse Fourier transform (13) can be read from right to left as a 'life history' of the singly scattered waves. The two terms in braces account for the propagation through an angular distance $\Delta_{\rm s}(\mathbf{s})$ from the source to the scatterer, and through an angular distance $\Delta_{\rm r}(\mathbf{r})$ from the scatterer to the receiver; the quantities $k_{n'}(\omega)$ and $k_n(\omega)$ are the wavenumbers of the fundamental or overtone modes propagating along these two great-circular paths. The term $S_{n'}(\omega)$ accounts for the radiation pattern of the waves excited by the source, $V_{nn'}(\mathbf{r}, \omega)$ is a surface wave scattering matrix that accounts for the conversion from mode n' to mode

n at the scatterer, and $R_n(\omega)$ accounts for the polarization of the waves that arrive at the receiver. The 3-D sensitivity of teleseismic S waves and surface-reflected SS, SSS, ... waves can be modelled by summing all Love and Rayleigh waves with mode numbers less than $n, n' \approx 20$. A significantly larger number of modes must be included to model the sensitivity of core-reflected phases such as ScS or ScS_2.

2.3 Traveltime sensitivity kernel

To relate the traveltime shift δT to the perturbation $\delta\beta(\mathbf{r})$ we substitute the representation (12) into (11). An interchange in the order of integration yields the result

$$\delta T = \int_{\oplus} K_T(\mathbf{r})\,\delta\beta(\mathbf{r})\,dV\,, \tag{14}$$

where

$$K_T(\mathbf{r}) = \frac{\displaystyle\int_{t_1}^{t_2} \dot{u}(t) K_u(\mathbf{r}, t)\,dt}{\displaystyle\int_{t_1}^{t_2} \ddot{u}(t) u(t)\,dt}\,. \tag{15}$$

The quantity $K_T(\mathbf{r})$ is the desired 3-D sensitivity kernel of a finite-frequency traveltime shift measured by cross-correlation of an observed and synthetic seismogram; the subscript T serves to distinguish this from the time-dependent waveform kernel $K_u(\mathbf{r}, t)$.

2.4 Differential traveltime kernel

The result (14)–(15) can be easily generalized to a differential traveltime shift measured by cross-correlation of two observed seismograms,

$$u_{\text{obs}}(t) = u(t) + \delta u(t) \quad \text{and} \quad v_{\text{obs}}(t) = v(t) + \delta v(t)\,. \tag{16}$$

The two signals $u_{\text{obs}}(t)$ and $v_{\text{obs}}(t)$ can either be the same phase, recorded at two closely spaced stations, or they can be two different phases, recorded at the same station. In the latter case, it is assumed that the waveforms have been processed so that they resemble each other; for example, it is necessary to Hilbert transform an S pulse prior to cross-correlation with SS, to account for the caustic phase shift of the latter (Hill 1974). The cross-correlation

$$C(\tau) = \int_{t_1}^{t_2} u_{\text{obs}}(t-\tau) v_{\text{obs}}(t)\,dt \tag{17}$$

can again be decomposed into a zeroth-order and a first-order term:

$$C(\tau) = c(\tau) + \delta c(\tau)\,, \tag{18}$$

where

$$c(\tau) = \int_{t_1}^{t_2} u(t-\tau) v(t)\,dt\,, \tag{19}$$

$$\delta c(\tau) = \int_{t_1}^{t_2} [u(t-\tau)\delta v(t) + \delta u(t-\tau) v(t)]\,dt\,. \tag{20}$$

The unperturbed cross-correlation in this case attains its maximum at the differential traveltime $\tau = \Delta T$ between the two phases in the spherical earth model. The perturbation $\delta\beta(\mathbf{r})$ shifts the position of this maximum by an amount $\delta\tau = \delta(\Delta T)$.

The Taylor series expansion of (18) about the spherical earth maximum is

$$\begin{aligned} C(\tau+\delta\tau) &= c(\tau) + \delta\tau\partial_\tau c(\tau) + \frac{1}{2}\,\delta\tau^2\partial_{\tau\tau}c(\tau) + \delta c(\tau) + \delta\tau\partial_\tau\delta c(\tau) \\ &= c(\tau) + \frac{1}{2}\,\delta\tau^2\partial_{\tau\tau}c(\tau) + \delta c(\tau) + \delta\tau\partial_\tau\delta c(\tau)\,, \end{aligned} \tag{21}$$

where we have once again used the unperturbed condition $\partial_\tau c(\tau) = 0$ to obtain the second equality. The shift in the maximum is obtained from the perturbed condition

$$\partial_{\delta\tau}\left[c(\tau) + \frac{1}{2}\,\delta\tau^2\partial_{\tau\tau}c(\tau) + \delta c(\tau) + \delta\tau\partial_\tau\delta c(\tau)\right] = 0\,. \tag{22}$$

This leads to a result identical to (10), with the argument zero replaced by the unperturbed lag τ:

$$\delta\tau = -\frac{\partial_\tau\delta c(\tau)}{\partial_{\tau\tau}c(\tau)}\,. \tag{23}$$

Upon making the identifications $\tau = \Delta T$ and $\delta\tau = \delta(\Delta T)$, we find

$$\delta(\Delta T) = \frac{\displaystyle\int_{t_1}^{t_2} [\dot{u}(t-\Delta T)\delta v(t) + \delta\dot{u}(t-\Delta T) v(t)]\,dt}{\displaystyle\int_{t_1}^{t_2} \ddot{u}(t-\Delta T) v(t)\,dt}\,, \tag{24}$$

where a dot again denotes differentiation with respect to time. The waveform perturbations $\delta u(t)$ and $\delta v(t)$ are related to $\delta\beta(\mathbf{r})$ via their respective kernels

$$\delta u(t) = \int_{\oplus} K_u(\mathbf{r}, t)\,\delta\beta(\mathbf{r})\,dV\,, \tag{25}$$

$$\delta v(t) = \int_{\oplus} K_v(\mathbf{r}, t)\,\delta\beta(\mathbf{r})\,dV\,. \tag{26}$$

Upon inserting (25)–(26) into (24) and interchanging the order of integration, we obtain the desired result,

$$\delta(\Delta T) = \int_{\oplus} K_{\Delta T}(\mathbf{r})\,\delta\beta(\mathbf{r})\,dV\,, \tag{27}$$

where

$$K_{\Delta T}(\mathbf{r}) = \frac{\displaystyle\int_{t_1}^{t_2} [\dot{u}(t-\Delta T) K_v(\mathbf{r}, t) + \dot{K}_u(\mathbf{r}, t-\Delta T) v(t)]\,dt}{\displaystyle\int_{t_1}^{t_2} \ddot{u}(t-\Delta T) v(t)\,dt}\,. \tag{28}$$

The quantity $K_{\Delta T}(\mathbf{r})$ is the 3-D sensitivity kernel for a differential traveltime shift measured by cross-correlation of two observed pulses $u_{\text{obs}}(t)$ and $v_{\text{obs}}(t)$.

2.5 Validity

By definition, the Born kernels $K_T(\mathbf{r})$ and $K_{\Delta T}(\mathbf{r})$ are the first Fréchet derivative of the traveltimes T and ΔT with respect to the 3-D shear wave speed heterogeneity $\delta\beta(\mathbf{r})$. Measured traveltime shifts δT and $\delta(\Delta T)$ will be well described by the local linearized relations (14) and (27) only if they are small compared to the dominant period of the cross-correlated waves. Larger traveltime shifts and cycle skips cannot be modelled using the Born approximation.

3 RECAPITULATION

Mindful of our obligation not to indulge in excessive regurgitation, we briefly reconsider a simple synthetic example from Marquering *et al.* (1998), which illustrates the principle of cross-correlation traveltime measurement. Fig. 1(a) shows a cross-sectional representation of a 3-D discretization of the mantle; the *S* and *SS* ray paths between a surface source and receiver separated by an epicentral distance $\Delta = 60^\circ$ are depicted by thick black lines. The spherical earth synthetic seismogram $u(t)$ obtained by surface wave summation for this source–receiver geometry is shown at the top of Fig. 1(b). The underlying traces in (b) show the waveform perturbations $\delta u_j(t)$ produced by a positive perturbation in shear wave speed, $\delta\beta(\mathbf{r}) > 0$, within each of the shaded parameter cells $j = 1$–9. Each such single-scatterer perturbation is a scaled, discretized measure of the 3-D waveform sensitivity kernel $K_u(\mathbf{r}_j, t)$ at the centroid $\mathbf{r}_j$ of the cell. Ray-plane cells situated just beneath the *SS* bounce point give rise to scattered waves that arrive in the *SS* time window, whereas cells near the turning point of the *S* wave give rise to scattered waves that arrive in the *S* time window. Figs 1(c) and (d) show a magnified view of the spherical earth seismogram $u(t)$, the perturbation $\delta u_7(t)$ and the sum seismogram $u(t) + \delta u_7(t)$ for a 10 per cent perturbation, $\delta\beta(\mathbf{r}_7)/\beta(r_7) = 10$ per cent. The principal effect of such a positive wave-speed perturbation in cell 7 is to produce an advance in the arrival time of the *S* wave, $\delta T < 0$, as expected.

Fig. 2 illustrates the mechanics of measuring this traveltime shift by means of cross-correlation. The unperturbed and perturbed seismograms $u(t)$ and $u(t) + \delta u_7(t)$ are duplicated in the top panel (a). The next panel (b) shows a magnified view of the two *S* waves; a 20 per cent cosine taper has been applied to each end to reduce the influence of energy arriving outside the time window. The cross-correlagram of the two windowed signals, shown in Fig. 2(c), has a maximum at $\delta\tau = -6.3$ s, corresponding to a traveltime advance of the perturbed *S* wave relative to the unperturbed one. Fig. 2(d) shows the optimum fit, with the spherical earth pulse $u(t)$ shifted backwards by 6.3 s. The superposition makes it clear that the perturbation has given rise to a slight alteration in the shape of the waveform; nevertheless, the aligned signals are quite similar, and the time shift $\delta T = -6.3$ s can be measured quite accurately. The dominant period of these decidedly non-impulsive *S* waves is approximately 50 s, eight times greater than the traveltime shift. This is the proper province of the Born approximation.

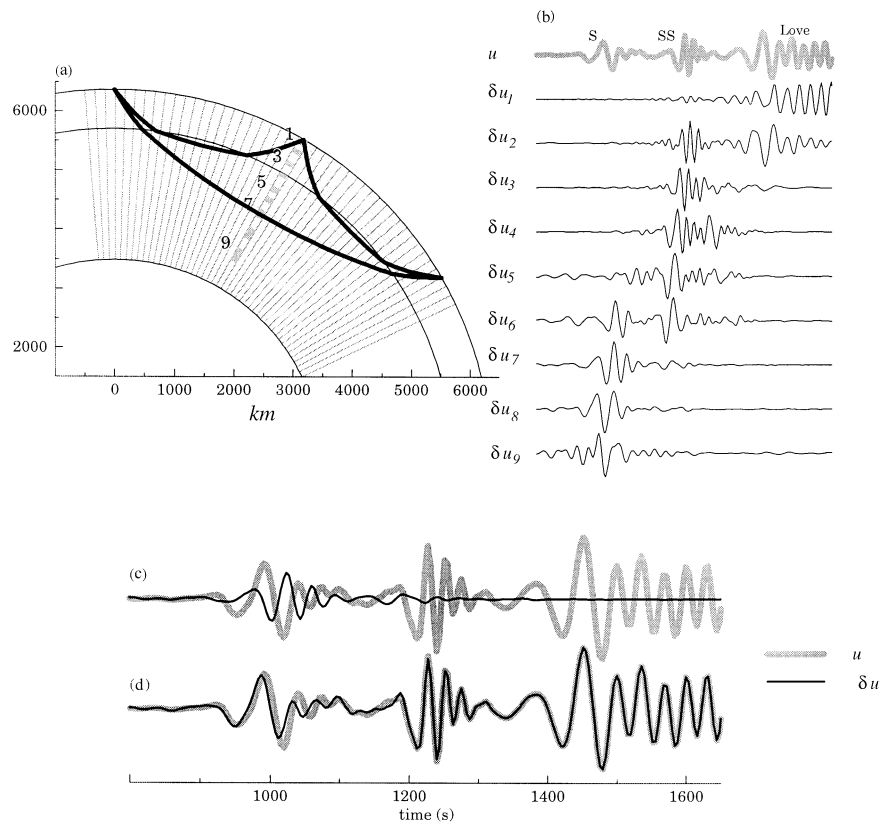

Figure 1. (a) Cross-section through the source, receiver and centre of the Earth. The ray-plane parameter cells $j = 1$–9 are shaded. (b) Thick grey line at top is the spherical earth synthetic seismogram $u(t)$ at an epicentral distance $\Delta = 60^\circ$, showing the *S*, *SS* and fundamental-mode Love waves. Thin lines are the individual Born 'scattergrams' $\delta u_j(t)$ resulting from a positive perturbation in shear wave speed, $\delta\beta(\mathbf{r}) > 0$, within each of the cells $j = 1$–9; all the plots are scaled to have the same maximum amplitude. (c) Unperturbed spherical earth seismogram $u(t)$ and 'scattergram' $\delta u_7(t)$ due to a perturbation in cell 7. (d) Superposition of the unperturbed and perturbed seismograms $u(t)$ and $u(t) + \delta u_7(t)$. The *SS* and Love waves are not strongly affected by the increase in the shear wave speed within cell 7; however, the *S* wave is speeded up, so that it arrives slightly earlier. The amplitude of the perturbation within a single cell needs to be large, $\delta\beta(\mathbf{r}_7)/\beta(r_7) \approx 10$ per cent, to produce a perturbation ΔT of this magnitude; nevertheless, this example illustrates how the addition of a scattered signal $\delta u(t)$ can result in a traveltime shift of the *S* wave.

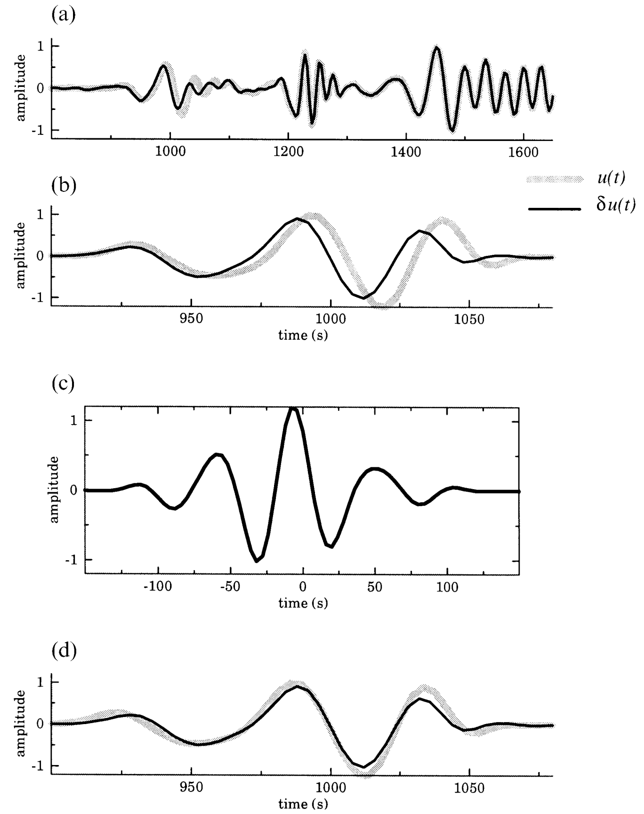

Figure 2. (a) Spherical earth synthetic seismogram $u(t)$ and perturbed seismogram $u(t)+\delta u_7(t)$ due to a positive perturbation in shear wave speed, $\delta\beta(\mathbf{r})>0$, in cell 7. (b) Blow-up of the unperturbed and perturbed S waves, during the windowed time interval $t=900$–1100 s; the advance in traveltime ΔT is clearly visible. (c) Cross-correlagram $C(t)$ of the two seismograms $u(t)$ and $u(t)+\delta u_7(t)$; the location of the maximum determines the traveltime shift, $\Delta T=-6.3$ s. (d) Superposition of $u(t)+\delta u_7(t)$ and the shifted spherical earth seismogram $u(t+\Delta T)$.

4 KERNEL CORNUCOPIA

In this section, we present a number of 3-D traveltime sensitivity kernels $K_T(\mathbf{r})$ and $K_{\Delta T}(\mathbf{r})$. For simplicity, we consider only *SH*-to-*SH* scattering, and restrict attention to an extremely simple, spherical earth model, with an unperturbed shear wave speed of the form

$$\beta(r)=\beta_0+b(r-a)\,. \tag{29}$$

The wave speed at the surface, linear rate of increase with depth, and radius of the earth are given, respectively, by $\beta_0=4446\ \mathrm{m\ s^{-1}}$, $b=1.53\times10^{-3}\ \mathrm{s^{-1}}$ and $a=6371$ km. More realistic spherical earth models have a number of additional complications, notably traveltime triplications, reflections and conversions associated with upper-mantle discontinuities. It is straightforward to allow for a change in wave type upon scattering, and compute the sensitivity kernels $K_T(\mathbf{r})$ and $K_{\Delta T}(\mathbf{r})$ for any compound wave in a more general earth model $\alpha(r)$, $\beta(r)$, $\rho(r)$. However, the pictorial results we are about to present are, at first sight, extremely counterintuitive; for this reason, we consider only *SH* waves in the constant-gradient model (29). The earthquake source in each of our examples is a vertical strike-slip fault, and the azimuth to the transverse-component receiver is perpendicular to strike; that is, it is in the direction of maximum *SH* radiation. All of the kernels $K_T(\mathbf{r})$ and $K_{\Delta T}(\mathbf{r})$ are, as a result, symmetric about the source–receiver ray plane.

4.1 *S* wave

In Fig. 3, we present a number of cross-sectional views of the 3-D traveltime sensitivity kernel $K_T(\mathbf{r})$ for a 0.01–0.06 Hz (17–100 s) S wave, at an epicentral distance $\Delta=40°$. The quantity actually plotted in this and all the following figures is the traveltime shift $\delta T(\mathbf{r})$ produced by a 10 per cent perturbation in the shear wave speed, $\delta\beta(\mathbf{r})/\beta(r)=10$ per cent, within a $1°\times1°\times100$ km parameter cell centred upon the point in question. Fig. 3(a) shows a vertical cross-section in the source–receiver plane; the geometrical ray path is depicted by the black and white line. Fig. 3(b) shows the off-path structure of the kernel on a series of parallel slices situated at distances 0.75°, 1.50°, 2.25° and 3.00° from the ray plane. Finally, Fig. 3(c) shows a cross-section in a direction perpendicular to the direction of propagation, at the turning point of the wave. The most striking observation that can be made from this ensemble of views is that the sensitivity of the traveltime of an S wave is *zero everywhere along its geometrical ray path.* The geometry of the kernel $K_T(\mathbf{r})$ resembles that of a hollow banana centred upon the ray; the cross-path shape resembles a doughnut. The observation that $K_T(\mathbf{r})\to0$ on the geometrical ray is implicit in the analyses of both Woodward (1992) and Yomogida (1992); however, neither of them emphasized the paradoxical character of this result.

It may not be remiss to re-emphasize that $K_T(\mathbf{r})$ describes the sensitivity of an infinitesimal traveltime shift ΔT measured by cross-correlation of the entire 0.01–0.06 Hz pulse. The very first-arriving, infinite-frequency waves certainly propagate along the geometrical ray path. The detailed shape of the cross-correlated pulse is, however, the result of interference between these first-arriving waves and later-arriving waves which scatter and diffract off wave speed heterogeneity $\delta\beta(\mathbf{r})$ in the vicinity of the geometrical ray path. From this point of view, it is not unreasonable that heterogeneity right on the ray path does not exert any influence upon the cross-correlation traveltime. Waves that are forward-scattered off ray path heterogeneity arrive at the same time as unscattered direct waves; for this reason, they affect the amplitude, but not the traveltime of the waveform. Since the 3-D *waveform* sensitivity kernel $K_u(\mathbf{r},t)$ describes the amplitude as well as the phase of $\delta u(t)$, it does *not* exhibit a minimum along the geometrical ray (Marquering *et al.* 1998). The hole in the middle is a characteristic feature only of the traveltime kernel $K_T(\mathbf{r})$.

4.2 Frequency dependence

Fig. 4 illustrates the effect of frequency upon the sensitivity kernel $K_T(\mathbf{r})$ of an S wave at an epicentral distance $\Delta=40°$. The top two plots again show the ray-plane and cross-path sections for a broad-band pulse, with frequencies in the range 0.01–0.06 Hz (periods between 17 and 100 s), the middle two plots show the kernel for a low-pass filtered wave, with frequencies in the range 0.01–0.02 Hz (periods between 50 and 100 s), and the lower two plots show the kernel for a high-pass filtered wave, with frequencies in the range 0.04–0.05 Hz (periods between 20 and 25 s). The effect of lowering the frequency content of the cross-correlated signals is to 'fatten'

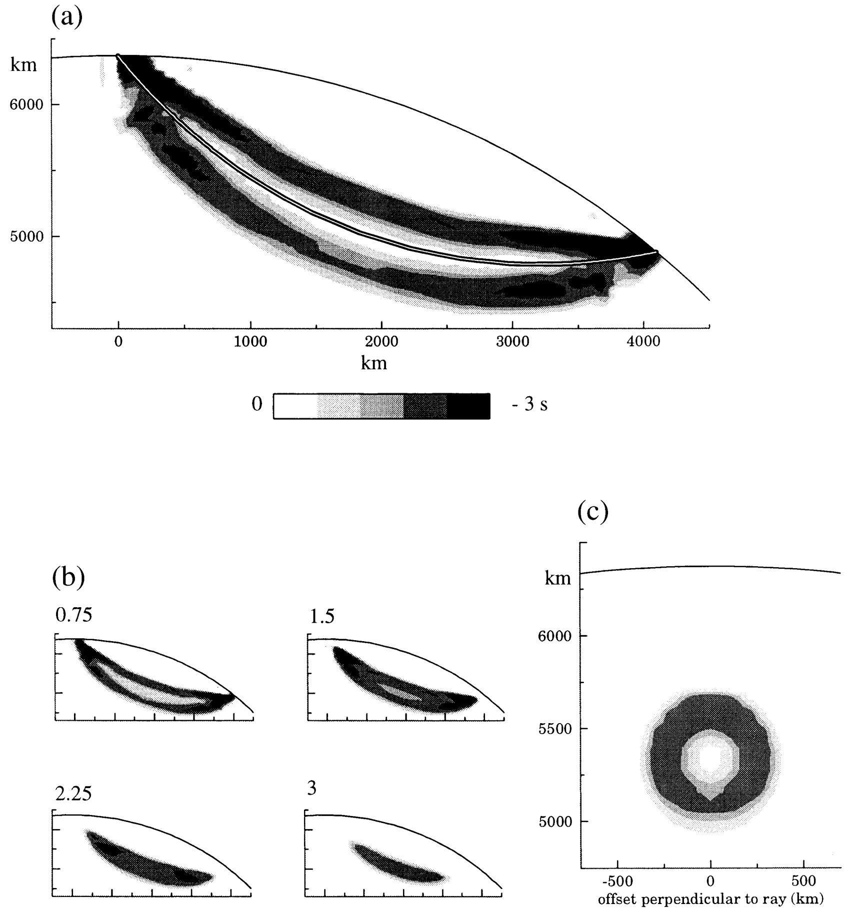

Figure 3. Cross-sections through the 3-D sensitivity kernel $K_T(\mathbf{r})$ for a 0.01–0.06 Hz (17–100 s period) S wave at an epicentral distance $\Delta = 40°$. (a) Ray-plane cross-section through the source, receiver and centre of the Earth. (b) Off-plane cross-sections at perpendicular distances $\Delta = 0.75°$, $\Delta = 1.50°$, $\Delta = 2.25°$ and $\Delta = 3.00°$ from the ray plane. (c) Perpendicular cross-section through the turning point at $\Delta = 20°$. Shading (black to white) shows the traveltime shift produced by a 10 per cent perturbation in shear wave speed, within a $1° \times 1° \times 100$ km cell, centred upon the plotted point. Note that the greyscale is one-sided: $-3\ \mathrm{s} \le \delta T(\mathbf{r}) \le 0$ s. The banana–doughnut character of the kernel is evident.

the banana, whereas the effect of increasing the frequency content is to 'slenderize' it. The relatively narrow passband in the high-frequency case also gives rise to a number of fringing sidebands (banana skins) with alternating signs of $K_T(\mathbf{r})$. These features are reminiscent of the first and higher-order Fresnel zones which characterize the constructive and destructive interference of strictly monochromatic waves. The cross-path width of the innermost banana with negative values, $K_T(\mathbf{r}) < 0$, closest to the ray is approximately the same for the broad-band 0.01–0.06 Hz wave as for the high-passed 0.04–0.05 Hz wave. This is an indication that the width of the traveltime kernel is governed by the highest frequencies in the cross-correlated phase. The main effect of including lower frequencies is to cancel out the higher-order Fresnel zones. The sensitivity kernel for a pulse dominated by extremely high frequencies would be an extremely skinny hollow banana, centred upon the geometrical ray. If the along-ray heterogeneities $\delta\beta(\mathbf{r})$ are wider than this banana, they will exert an influence upon the traveltime ΔT in accordance with ray theory, eq. (2).

4.3 2-D ray-plane sensitivity

A number of investigators have presented schemes for computing and implementing the 2-D sensitivity of a seismic traveltime or other 'generalized data functional' within the source–receiver geometrical ray plane (Li & Tanimoto 1993; Vasco & Majer 1993; Li & Romanowicz 1995; Marquering & Snieder 1995, 1996; Zhao & Jordan 1998; Katzman *et al.* 1998). All such 2-D formulations are grounded upon the (often implicit) assumption that the 3-D heterogeneity $\delta\beta(\mathbf{r})$ is smooth in the direction perpendicular to the ray plane. It is possible to find the 2-D ray-plane sensitivity by means of a stationary-phase evaluation of the cross-path integral in eq. (14). This leads to a representation of the form

$$\delta T = \int_\Sigma K_T^{\mathrm{2D}}(\mathbf{r})\, \delta\beta(\mathbf{r})\, d\Sigma\,, \tag{30}$$

where the integration is over all points $\mathbf{r}$ on the ray plane Σ. The 2-D traveltime kernel $K_T^{\mathrm{2D}}(\mathbf{r})$ is related to the corresponding waveform kernel $K_u^{\mathrm{2D}}(\mathbf{r}, t)$ by an equation analogous to (15):

$$K_T^{\mathrm{2D}}(\mathbf{r}) = \frac{\displaystyle\int_{t_1}^{t_2} \dot{u}(t) K_u^{\mathrm{2D}}(\mathbf{r}, t)\, dt}{\displaystyle\int_{t_1}^{t_2} \ddot{u}(t) u(t)\, dt}\,. \tag{31}$$

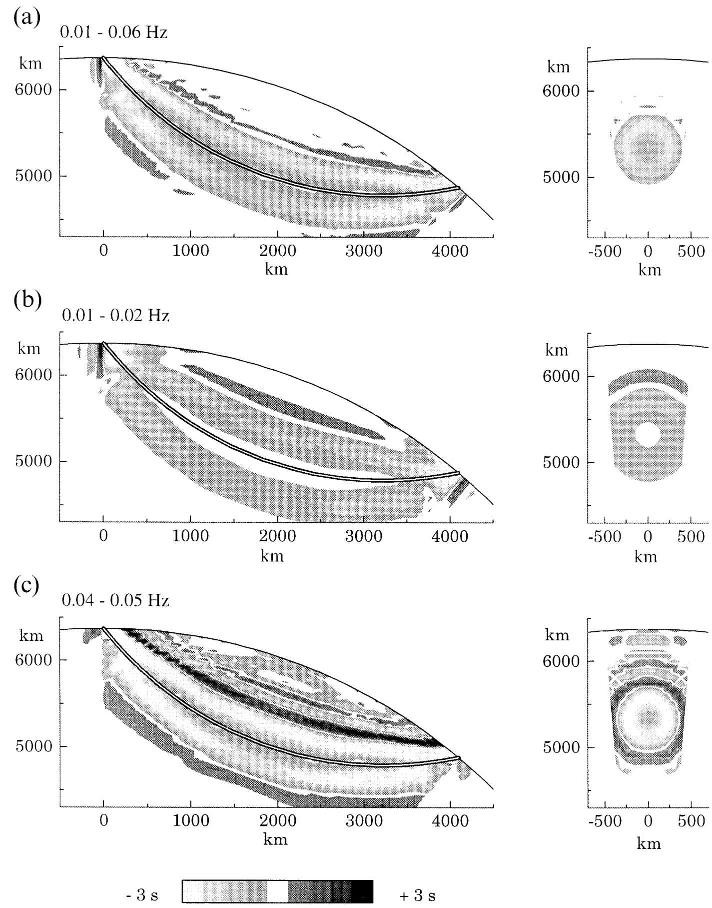

Figure 4. Frequency dependence of the S wave traveltime sensitivity kernel $K_T(\mathbf{r})$ at an epicentral distance $\Delta=40°$. The three frequency bands are (a) 0.01–0.06 Hz, (b) 0.01–0.02 Hz and (c) 0.04–0.05 Hz. The bottom two kernels are computed by band-pass filtration of $u(t)$ and $K_u(\mathbf{r}, t)$ prior to evaluation of the ratio (14). A vertical ray-plane cross-section and a perpendicular cross-section through the turning point are shown in each case. To depict the fringing sidebands, we are compelled to use a two-sided greyscale in this case: $-3\ \mathrm{s}\leq\delta T(\mathbf{r})\leq 3$ s. All of the kernels are nearly zero (white and medium-grey) in the vicinity of the geometrical ray.

An explicit expression for $K_u^{\mathrm{2D}}(\mathbf{r}, t)$ is derived in Appendix B of Marquering *et al.* (1998):

$$K_u(\mathbf{r}, t)=\frac{1}{\pi}\mathscr{Re}\int_0^{\infty}\sum_{n,n'}2k_n^{-1}(\omega)R_n(\omega)V_{nn'}(\mathbf{r}, \omega)S_{n'}(\omega)$$

$$\times\left\{\frac{\exp i\,[k_n(\omega)\Delta_{\mathrm{r}}(\mathbf{r})+k_{n'}(\omega)\Delta_{\mathrm{s}}(\mathbf{r})+3\pi/4]}{\sqrt{\frac{1}{2}\,\pi k_{n'}(\omega)\sin\Delta}}\right\}$$

$$\times\exp(-i\omega t)\,d\omega\,, \tag{32}$$

where $\Delta=\Delta_{\mathrm{s}}(\mathbf{r})+\Delta_{\mathrm{r}}(\mathbf{r})$ is the source–receiver epicentral distance. Fig. 5 compares the 2-D traveltime kernel $K_T^{\mathrm{2D}}(\mathbf{r})$ with the ray-plane cross-section through the 3-D kernel $K_T(\mathbf{r})$ for an S wave at a distance $\Delta=40°$. It is evident that the two kernels are fundamentally different; in particular, the 2-D kernel does *not* exhibit zero sensitivity along the geometrical ray. This difference can be traced to the additional $\pi/4$ phase factor that arises in the cross-path stationary-phase integration; physically, the difference is due to the interference of waves scattered off the cylindrically symmetric heterogeneity $\delta\beta(\mathbf{r})$ on either side of the ray plane. These off-plane scattered waves do not simply propagate along the geometrical ray path; hence, they can contribute to the traveltime shift ΔT. Inspection of current 3-D tomographic models of the earth does not give us any reason to expect that $\delta\beta(\mathbf{r})$ should be significantly smoother in the direction perpendicular to an arbitrary ray plane than within it. In our opinion, this is ample justification for using 3-D rather than 2-D sensitivity kernels in the future.

4.4 *SS* wave

The *SS* wave, which reflects once off the surface of the Earth, is generally one of the most clearly observed shear wave phases following a shallow-focus earthquake. Recent analyses have pointed out a number of complications associated with this phase (Paulssen & Stutzmann 1996; Neele *et al.* 1997); nevertheless, it is an important source of data, because of its ability to sample shallow heterogeneity beneath the ray-theoretical surface bounce point in regions which may not be well sampled by subsource and subreceiver S waves. Fig. 6 shows a number of cross-sectional views of the 3-D sensitivity kernel $K_T(\mathbf{r})$ for an *SS* wave at an epicentral distance $\Delta=80°$. It is evident that the kernel geometry is considerably more complicated than that of the direct S wave. The ray-plane cross-section in Fig. 6(a) reveals that a cross-correlation traveltime measurement exhibits zero sensitivity along the ray between the

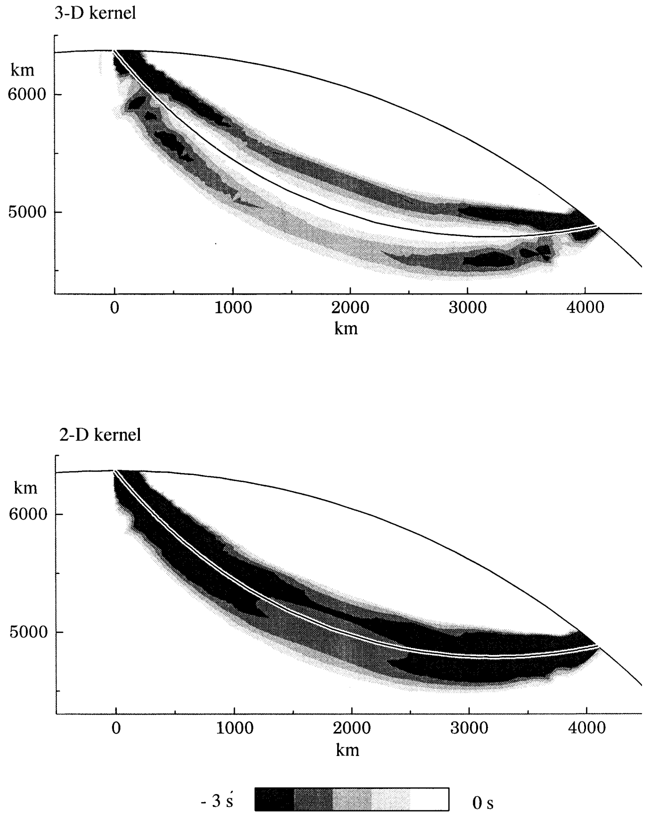

Figure 5. Comparison of the 3-D (top) and 2-D (bottom) sensitivity kernels for a 0.01–0.06 Hz (17–100 s) *S* wave at an epicentral distance $\Delta = 40°$. The 2-D kernel $K_T^{2D}(\mathbf{r})$ is strictly appropriate only if the heterogeneity $\delta\beta(\mathbf{r})$ is cylindrically symmetric across the ray plane (that is, uniform and infinite in extent in and out of the page).

source and the receiver-to-source caustic, at $\Delta \approx 30°$, as well as between the receiver and the source-to-receiver caustic, at $\Delta \approx 50°$. Between these two caustics, and in particular in the vicinity of the surface bounce point at $\Delta = 40°$, there is a local maximum in sensitivity, as illustrated by the large white area in the perpendicular cross-section in Fig. 6(b). The off-plane sensitivity on a series of parallel slices at perpendicular distances 2.25°, 4.50°, 6.75° and 9.00° is depicted in Fig. 6(c). The bottom panel, Fig. 6(d), shows a map view of the near-surface sensitivity. The saddle-shaped near-surface pattern is a consequence of the minimax nature of the *SS* phase (Neele & Snieder 1992). Waves that scatter off in-plane heterogeneity to the 'east' or 'west' of the bounce point arrive earlier than the geometrical *SS* wave, whereas those that scatter off out-of-plane heterogeneity to the 'north' or 'south' arrive after the *SS* wave. The large magnitude of $K_T(\mathbf{r})$ in the four tails of the 'X' is an indication that near-surface heterogeneity $\delta\beta(\mathbf{r})$ situated more than 15° from the bounce point can exert a significant influence upon the traveltime of an *SS* wave. Finally, we would like to call attention to the presence of the fringing regions in which $K_T(\mathbf{r}) > 0$, denoted by the dark shading in Figs 6(b) and (d). A positive wave speed perturbation, $\delta\beta(\mathbf{r}) > 0$, in any such region results in a traveltime delay, $\delta T > 0$. This apparently acausal sensitivity is a sideband feature analogous to the outer-Fresnel-zone sidebands in Fig. 4(c); note, however, that the 3-D kernel $K_T(\mathbf{r})$ in Fig. 6 is for a broad-band 0.01–0.06 Hz (17–100 s) *SS* pulse. The pronounced sideband structure in the vicinity of the surface reflection point and all the other geometrical complexities of $K_T(\mathbf{r})$ are the result of the complex interference of the various scattered waves.

4.5 Love wave

Because of their large amplitude, their ability to sample the Earth's shallow heterogeneity over extensive geographical regions, and their dispersive properties which provide some depth resolution, fundamental-mode surface waves have been utilized since the time of Gutenberg (1924) to constrain the structure of the crust and upper mantle. The most widely used data in modern global inversion studies are measurements of the path-averaged perturbation in the wavenumber $\overline{\delta k}(\omega)$ or phase speed $\overline{\delta c}(\omega)$ of a wave of frequency ω (Trampert & Woodhouse 1995, 1996; Zhang & Lay 1996; Laske & Masters 1996; Ekström *et al.* 1997). The relative wavenumber and phase speed perturbations are related by

$$\frac{\overline{\delta k}(\omega)}{k(\omega)} = -\frac{\overline{\delta c}(\omega)}{c(\omega)}\,. \tag{33}$$

In the JWKB approximation, which is generally used as the basis for inversion, a measurement of $\overline{\delta k}(\omega)$ or $\overline{\delta c}(\omega)$ depends only upon the laterally averaged depth-dependent structure beneath the source–receiver path,

$$\overline{\delta\beta}(r) = \frac{1}{\Delta}\int_{\text{path}} \delta\beta(r, \theta, \phi)\, d\Delta\,, \tag{34}$$

where θ is the colatitude and ϕ is the longitude. We can use our Born cross-correlation formalism to assess the *3-D sensitivity* of a surface wave by reinterpreting $\overline{\delta k}(\omega)$, $\overline{\delta c}(\omega)$ in terms of a frequency-dependent shift $\delta T(\omega)$ in the *phase delay*, given to first order by

$$\omega\, \delta T(\omega) = \overline{\delta k}(\omega)\, \Delta = -\omega c^{-2}(\omega)\, \overline{\delta c}(\omega)\, \Delta\,. \tag{35}$$

This phase-delay perturbation is related to the perturbation $\delta\beta(\mathbf{r})$ in the shear wave speed via a frequency-dependent kernel:

$$\delta T(\omega) = \int_{\oplus} K_T(\mathbf{r}; \omega)\, \delta\beta(\mathbf{r})\, dV\,, \tag{36}$$

where

$$K_T(\mathbf{r}; \omega) = \frac{\int_{t_1}^{t_2} \dot{u}(t; \omega) K_u(\mathbf{r}, t; \omega)\, dt}{\int_{t_1}^{t_2} \ddot{u}(t; \omega) u(t; \omega)\, dt}\,. \tag{37}$$

Here we use the admittedly vague notation $u(t; \omega)$ and $K_u(\mathbf{r}, t; \omega)$ to denote the result of applying a narrow-band filter centred upon ω to the surface wave portions of $u(t)$ and $K_u(t)$, respectively. Fig. 7 shows the phase-delay sensitivity kernel $K_T(\mathbf{r}; \omega)$ for the fundamental-mode Love wave at an epicentral distance $\Delta = 60°$, computed in this manner. The 3-D sensitivity of 0.01–0.02 Hz (50–100 s) Love waves is shown in Fig. 7(a), whilst the sensitivity of 0.04–0.05 Hz (20–25 s) waves is shown in Fig. 7(b). The most noteworthy feature of $K_T(\mathbf{r}; \omega)$ is its remarkable cross-path width. In fact, the sensitivity to geographical structure off the geometrical ray path is several times greater than the depth sensitivity; this is evident in the vertical cross-sections, which are one-to-one. Note, furthermore, that the sensitivity is *not zero* along the surface wave ray;

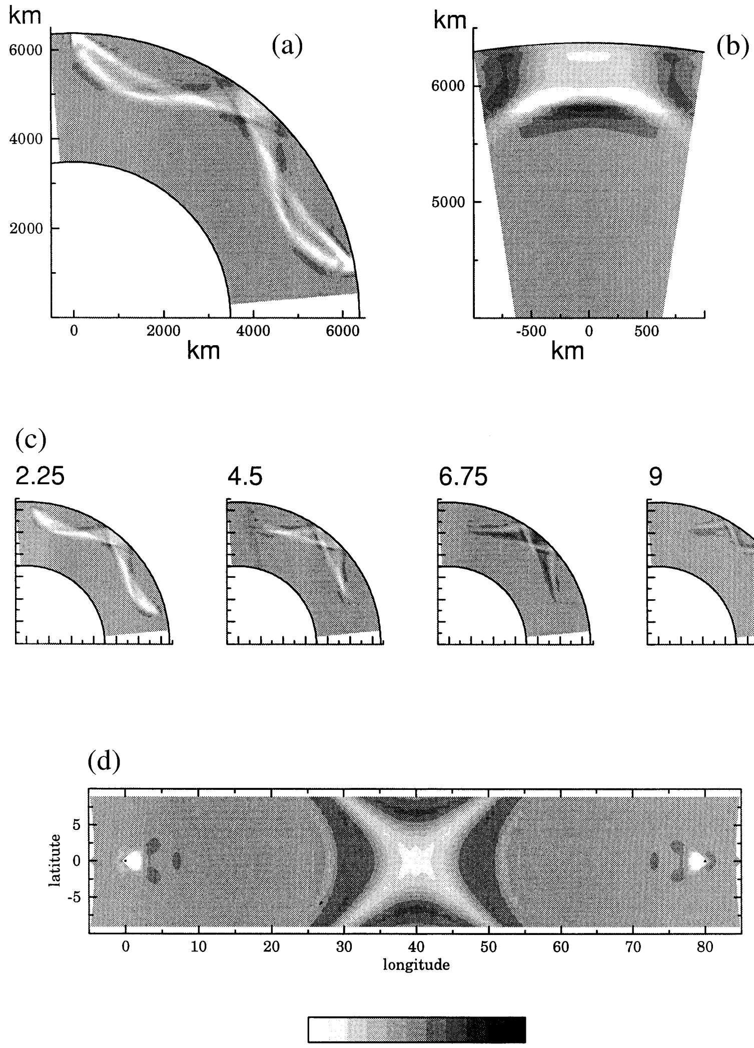

Figure 6. Cross-sections through the 3-D sensitivity kernel $K_T(\mathbf{r})$ for a 0.01–0.06 Hz (17–100 s) *SS* wave at an epicentral distance $\Delta = 80°$. (a) Ray-plane cross-section. (b) Perpendicular cross-section through the surface reflection point at $\Delta = 40°$. (c) Off-plane cross-sections at perpendicular distances $\Delta = 2.25°$, $\Delta = 4.50°$, $\Delta = 6.75°$ and $\Delta = 9.00°$ from the ray plane. (d) Map-view cross-section at a fixed radius near the Earth's surface. Note that yet a third greyscale is used in this figure, ranging from $\delta T(\mathbf{r}) = -3$ s (white) to $\delta T(\mathbf{r}) = 3$ s (black). Near the source ($0° \le \Delta \le 30°$) and the receiver ($50° \le \Delta \le 80°$) the sensitivity is nearly zero (medium-grey) along the geometrical ray.

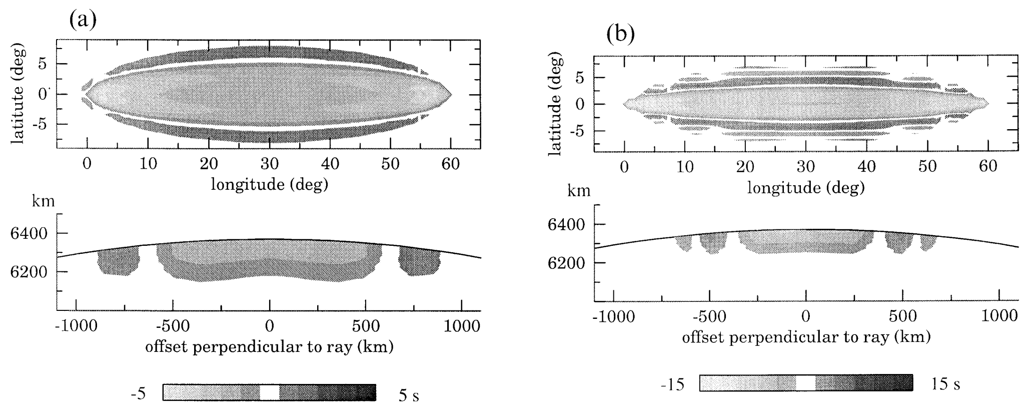

Figure 7. Sensitivity kernel $K_T(\mathbf{r};\,\omega)$ of the fundamental-mode Love surface wave at an epicentral distance $\Delta = 60°$. (a) Frequency band 0.01–0.02 Hz (50–100 s period). (b) Frequency band 0.04–0.05 Hz (20–25 s period). Lower panels show map-view cross-sections at the Earth's surface, and upper panels show perpendicular cross-sections halfway between the source and receiver ($\Delta = 30°$). The outer-Fresnel-zone sidebands of the high-frequency kernel are more pronounced than those of the low-frequency kernel, because of the smaller fractional width of the bandpass $\Delta\omega/\omega$. Note the two-sided greyscales, with white (zero sensitivity) in the middle.

this is a consequence of the 2-D rather than 3-D character of the wave propagation. Both the depth sensitivity and the geographical sensitivity are reduced as the frequency of the wave is increased. The former phenomenon is, of course, well known, and is frequently exploited to invert 2-D maps of surface wave phase speed $\delta c(\theta, \phi, \omega)$ for the 3-D wave speed perturbation $\delta\beta(\mathbf{r})$. The 3-D kernels $K_T(\mathbf{r}; \omega)$ presented here can be used to invert directly for $\delta\beta(\mathbf{r})$ without producing intermediary maps of $\delta c(\theta, \phi, \omega)$.

4.6 Differential kernels

Differential traveltimes are a popular source of data in both global and regional inversion studies because they are thought to provide strong single-path constraints upon the location of the heterogeneity $\delta\beta(\mathbf{r})$. Thus, for example, teleseismic traveltime variations across a seismic network or array are frequently used to invert for structure beneath the array; the effect of near-source and deep-mantle variations $\delta\beta(\mathbf{r})$ is considered to be negligible because those portions of the ray paths are so similar (e.g. Aki *et al.* 1977; Humphreys *et al.* 1984; VanDecar & Crosson 1990). Likewise, *SS–S* traveltime variations are often ascribed to heterogeneity $\delta\beta(\mathbf{r})$ in the vicinity of the surface reflection point because of the similarity of the near-source and near-receiver ray paths (e.g. Kuo *et al.* 1987; Sheehan & Solomon 1991; Woodward & Masters 1991). In this section, we show how the 3-D differential traveltime sensitivity kernel $K_{\Delta T}(\mathbf{r})$ enables us to quantify the notion that 'ray path similarity implies cancellation'.

Fig. 8(a) depicts the sensitivity kernel $K_{\Delta T}(\mathbf{r})$ for a differential traveltime measurement made by cross-correlating two 0.01–0.06 Hz (17–100 s) *S* waves, recorded on the same azimuth, at epicentral distances $\Delta_1 = 61°$ and $\Delta_2 = 62°$. It is evident that $\Delta T = T_2 - T_1$ is primarily sensitive to wave speed variations $\delta\beta(\mathbf{r})$ in the vicinity of this two-station array; however, due to the finite-frequency 'doughnut' geometry, the 3-D sensitivity is more complicated than might be expected on the basis of geometrical ray theory. Fig. 8(b) shows the differential sensitivity of the *SS* wave, recorded at the same two stations. The strongest sensitivity is once again in the vicinity of the array; however, the cancellation along the remainder of the path is not as thorough as in the case of the *S* waves, even though the geometrical ray paths are closer together. Finally, in Fig. 8(c) we show the 3-D sensitivity kernel for a 0.01–0.06 Hz (17–100 s) *SS–S* differential traveltime measurement, at an epicentral distance $\Delta = 60°$. As expected, $K_{\Delta T}^{SS-S}(\mathbf{r})$ looks like a superposition $K_T^{SS}(\mathbf{r}) - K_T^{S}(\mathbf{r})$ of the individual *SS* and *S* kernels; it is negative in the vicinity of the *SS* bounce point and in a near-source and near-receiver 'half-banana' skin surrounding the *SS* ray, and it is positive in the banana skin surrounding the doughnut hole along the *S* ray. The most noteworthy feature is, however, the magnitude of the kernel in the vicinity of the source and receiver; in fact, $K_{\Delta T}^{SS-S}(\mathbf{r})$ attains its maximum amplitude there, because of the divergent factors $1/\sqrt{\sin\Delta_s(\mathbf{r})}$ and $1/\sqrt{\sin\Delta_r(\mathbf{r})}$ in (12). Though large, the near-source and near-receiver sensitivity is rapidly alternating between positive and negative (black and white). This highlights the fundamental character of an *SS–S* differential traveltime measurement; only if $K_{\Delta T}^{SS-S}(\mathbf{r})$ samples a *sufficiently smooth* perturbation $\delta\beta(\mathbf{r})$ will 'similar ray path' cancellation occur. In fact, many earthquakes occur in subduction zones, where the gradients in $\delta\beta(\mathbf{r})$ are particularly

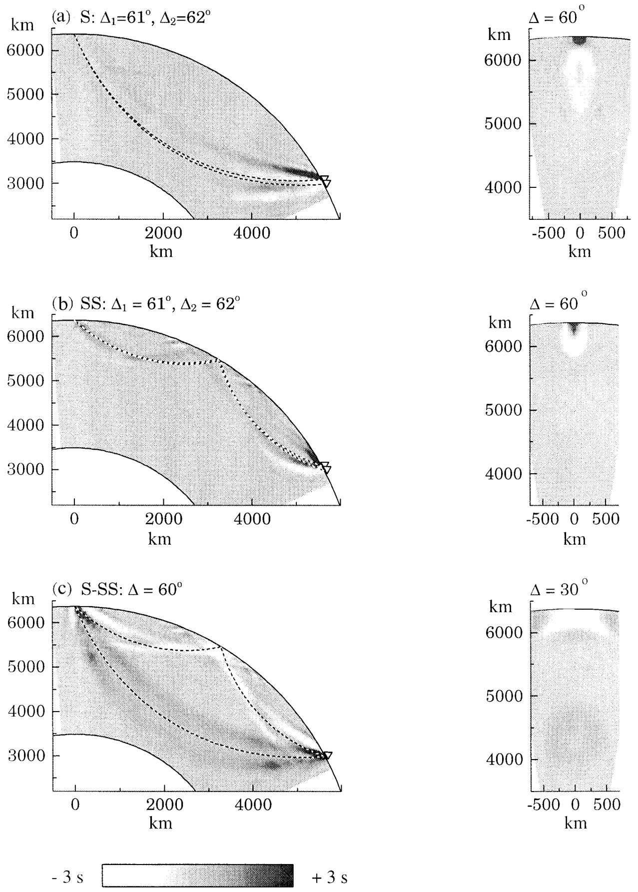

Figure 8. Differential traveltime sensitivity kernels $K_{\Delta T}(\mathbf{r})$. Left panel shows a ray-plane cross-section, and right panel shows a perpendicular cross-section at the indicated epicentral distance in each case. (a) 0.01–0.06 Hz (17–100 s period) *S* wave recorded at two equi-azimuth stations, situated at distances $\Delta = 61°$ and $\Delta = 62°$. (b) 0.01–0.06 Hz (17–100 s period) *SS* wave recorded at the same two closely spaced stations. (c) 0.01–0.06 Hz (17–100 s period) *SS–S* differential kernel at $\Delta = 60°$. Note the two-sided greyscale, ranging from $\delta T(\mathbf{r}) = -3$ s (white) to $\delta T(\mathbf{r}) = 3$ s (black).

pronounced. Arguments about the geographical origin of *SS–S* traveltime shifts can be avoided by utilizing the 3-D sensitivity kernel $K_{\Delta T}^{SS-S}(\mathbf{r})$ in future global inversions.

5 CONCLUSIONS

Geometrical ray theory has been the cornerstone of seismology for most of this century; it has proven useful in a myriad of applications, including earthquake location and tomography. Many current 3-D models of the interior structure of the Earth are based upon the ray-theoretical interpretation of body wave traveltime variations. Geometrical ray theory is, however, only valid if the scale length of the Earth's 3-D heterogeneity is much greater than the seismic wavelength. Cross-correlation traveltimes are often measured using intermediate-period and long-period waves, which have wavelengths of the order of 100–1000 km. Current global tomographic models exhibit wave speed variations with comparable scale lengths. The quest to resolve finer-scale details of the Earth's deep interior is certain to continue; it is inevitable that 3-D sensitivity kernels such as those developed here must play an important tomographic role in the future. We have restricted attention to an extremely simple special case—*SH* waves excited by a surface-focus vertical strike-slip fault in a constant-gradient earth model—for expositional clarity. It is straightforward to extend the results presented here to account for a general moment tensor source, compressional wave speed and density heterogeneity, and *S*-to-*P* and *P*-to-*S* scattering. Obviously, more realistic earth models with upper-mantle discontinuities will have even more complicated 3-D sensitivity kernels $K_T(\mathbf{r})$ and $K_{\Delta T}(\mathbf{r})$.

ACKNOWLEDGMENTS

We are grateful to Thomas Meier for writing the initial version of the surface wave coupling software, to Shu-Huei Hung and Li Zhao for several helpful discussions, and to Steve Ward for his editorial assistance. Financial support for this work has been provided by the National Science Foundation under Grants EAR-9505677 and EAR-9526372.

REFERENCES

Aki, K., Christoffersson, A. & Husebye, E.S., 1977. Determination of the three-dimensional seismic structure of the lithosphere, *J. geophys. Res.,* **82,** 277–296.

Ekström, G., Tromp, J. & Larson, E.W.F., 1997. Measurements and global models of surface wave propagation, *J. geophys. Res.,* **102,** 8137–8157.

Gutenberg, B., 1924. Dispersion und Extinktion von seismischen Oberflächenwellen und der Aufbau der obersten Erdschichten, *Physikalische Zeitschrift,* **25,** 377–382.

Hill, D., 1974. Phase shift and pulse distortion in body waves due to internal caustics, *Bull. seism. Soc. Am.,* **64,** 1733–1742.

Humphreys, E., Clayton, R.W. & Hager, B.H., 1984. A tomographic image of mantle structure beneath southern California, *Geophys. Res. Lett.,* **11,** 625–627.

Katzman, R., Zhao, L. & Jordan, T.H., 1998. High resolution, two-dimensional vertical tomography of the central Pacific using ScS reverberations and frequency-dependent travel times, *J. geophys. Res.,* **103,** 17 933–17 971.

Kuo, B.-Y., Forsyth, D.W. & Wysession, M., 1987. Lateral heterogeneity and azimuthal anisotropy in the North Atlantic determined from *SS–S* differential travel times, *J. geophys. Res.,* **92,** 6421–6436.

Laske, G. & Masters, G., 1996. Constraints on global phase velocity maps from long-period polarization data, *J. geophys. Res.,* **101,** 16 059–16 075.

Li, X.-D. & Romanowicz, B., 1995. Comparison of global waveform inversions with and without considering cross-branch modal coupling, *Geophys. J. Int.,* **121,** 695–709.

Li, X.-D. & Tanimoto T., 1993. Waveforms of long-period body waves in a slightly aspherical Earth model, *Geophys. J. Int.,* **112,** 92–102.

Marquering, H. & Snieder, R., 1995. Surface-wave mode coupling for efficient forward modelling and inversion of body-wave phases, *Geophys. J. Int.,* **120,** 186–208.

Marquering, H. & Snieder, R., 1996. Shear-wave velocity structure beneath Europe, the northeastern Atlantic and western Asia from waveform inversions including surface-wave mode coupling, *Geophys. J. Int.,* **127,** 283–304.

Marquering, H., Nolet, G. & Dahlen, F.A., 1998. Three-dimensional waveform sensitivity kernels, *Geophys. J. Int.,* **132,** 521–534.

Neele, F. & Snieder, R., 1992. Topography of the 400 km discontinuity from observations of long-period $P_{400}P$ phases, *Geophys. J. Int.,* **109,** 670–682.

Neele, F., De Regt, H. & VanDecar, J., 1997. Gross errors in upper-mantle discontinuity topography from underside reflection data, *Geophys. J. Int.,* **129,** 194–204.

Paulssen, H. & Stutzmann, E., 1996. On PP-P differential travel time measurements, *Geophys. Res. Lett.,* **23,** 1833–1836.

Sheehan, A. & Solomon, S., 1991. Joint inversion of shear wave travel time residuals and geoid and depth anomalies for long-wavelength variations in upper mantle temperature and composition along the Mid-Atlantic Ridge, *J. geophys. Res.,* **96,** 19 981–20 009.

Trampert, J. & Woodhouse, J.H., 1995. Global phase velocity maps of Love and Rayleigh waves between 40 and 150 seconds, *Geophys. J. Int.,* **122,** 675–690.

Trampert, J. & Woodhouse, J.H., 1996. High resolution global phase velocity distribution, *Geophys. Res. Lett.,* **23,** 21–24.

VanDecar, J. & Crosson, R., 1990. Determination of teleseismic relative phase arrival times using multi-channel cross-correlation and least squares, *Bull. seism. Soc. Am.,* **80,** 150–159.

Vasco, D.W. & Majer, E.L., 1993. Wavepath traveltime tomography, *Geophys. J. Int.,* **115,** 1055–1069.

Woodward, M.J., 1992. Wave-equation tomography, *Geophysics,* **57,** 15–26.

Woodward, R.L. & Masters, G., 1991. Global upper mantle structure from long-period differential travel times, *J. geophys. Res.,* **96,** 6351–6377.

Yomogida, K., 1992. Fresnel zone inversion for lateral heterogeneities in the Earth, *Pageoph.,* **138,** 391–406.

Zhang, Y.-S. & Lay, T., 1996. Global surface wave phase velocity variations, *J. geophys. Res.,* **101,** 8415–8436.

Zhao, L. & Jordan, T.H., 1998. Sensitivity of frequency-dependent travel times to laterally heterogeneous, anisotropic Earth structure, *Geophys. J. Int.,* **133,** 683–704.